ChemPubSoc Europe
DOI: 10.1002/celc.201600183
CHEMELECTROCHEM Articles

$NiCo_2S_4$ Nanosheets Grown on 3D Networks of Nitrogen-Doped Graphene/Carbon Nanotubes: Advanced Anode Materials for Lithium-Ion Batteries

Longsheng Zhang,[a] Lizeng Zuo,[a] Wei Fan,*[b] and Tianxi Liu*[a, b]

To meet the requirements of high-performance lithium-ion batteries (LIBs), a new class of electrode materials with favorable nanostructures is highly desirable. Recently, metal sulfides have been intensively studied as promising anode materials for LIBs because of their high lithium storage capacity. Among them, ternary metal sulfides can provide much higher electrochemical activity and energy storage performance than binary metal sulfides or their oxide counterparts, which makes them outstanding candidates as anode materials for next-generation LIBs. In this work, hierarchical nanostructured hybrids of $NiCo_2S_4$ nanosheets uniformly grown on nitrogen-doped graphene/carbon nanotube networks ($NiCo_2S_4$/NGC) have been easily prepared as novel anode materials for LIBs. Benefiting from the synergistic effects between $NiCo_2S_4$ nanosheets and conductive NGC networks, the optimized $NiCo_2S_4$/NGC hybrid exhibits greatly enhanced electrochemical performance with high initial charge capacity of 1225.4 mA h g^{-1} at a current density of 0.2 A g^{-1} and excellent cycling stability with 89% capacity retention after 100 cycles. Moreover, its capacity can be retained at 574.8 mA h g^{-1} after 100 cycles even at a current density of 5 A g^{-1}, demonstrating its exceptionally high rate performance.

1. Introduction

The ever-increasing demand for efficient energy storage has led to the development of rechargeable lithium-ion batteries (LIBs) with high energy density and long cycling life.[1] Currently, graphite is the most widely used anode material for LIBs, but it cannot fully meet the energy density requirements for next-generation LIBs because of its relatively low theoretical specific capacity (372 mA h g^{-1}).[2] This concern has driven the search for alternative anode materials with high specific capacity and good cycling stability.[3]

Recently, a variety of transition-metal sulfides (e.g. cobalt sulfides, nickel sulfides, tin sulfides, and ternary nickel cobalt sulfides) have been extensively studied as a new class of anode materials for next-generation LIBs because of their high theoretical capacities.[4–7] In particular, benefiting from the richer redox reactions provided by both nickel and cobalt ions, ternary nickel cobalt sulfides ($NiCo_2S_4$) can exhibit better electrochemical energy storage performance than binary metal sulfides (nickel sulfide or cobalt sulfide).[8–12] Additionally, $NiCo_2S_4$ has been shown to have excellent electrical conductivity, at least two orders of magnitude higher than that of the oxide counterpart ($NiCo_2O_4$), because the electronegativity of sulfur is much lower than that of oxygen.[13–15] However, the large volumetric expansion and contraction during the lithiation/delithiation process would result in serious pulverization of $NiCo_2S_4$ electrodes, leading to rapid capacity fade and inferior cycling performance.[16] Furthermore, self-aggregation of $NiCo_2S_4$ nanomaterials often makes it difficult to realize full lithiation of their internal portions and results in decreased lithium storage performance.[17–19]

To address these issues, various approaches have been established to improve the structural stability and enhance the cycling capacities of $NiCo_2S_4$-based anode materials. An effective approach is to fabricate nanostructured $NiCo_2S_4$ materials and confine them within conductive matrices, which can effectively improve the utilization of active materials by reducing the self-aggregation of $NiCo_2S_4$ nanomaterials and mitigate their volumetric change, leading to enhanced structural stability and electrochemical cycling performance.[20–24] Compared with other carbonaceous materials, graphene has attracted great attention as an ideal matrix to disperse and confine active materials because of its unique structures, large specific surface area, and superior electrical conductivity.[25–27] In recent years, chemical substitutional doping (e.g. sulfur, boron, and nitrogen doping) has been used to further enhance the properties of graphene.[28] Notably, nitrogen-doped (N-doped) graphene has been shown to be particularly effective in modulating the electronic properties of graphene, which is an excellent template for synthesis of active electrode materials.[29] Nevertheless, irreversible restacking of graphene sheets due to the strong interlayer π-π stacking and van der Waals interaction seriously hampers the utilization of the great potential of gra-

[a] L. Zhang, L. Zuo, Prof. T. Liu
State Key Laboratory of Molecular Engineering of Polymers
Department of Macromolecular Science, Fudan University
Shanghai 200433 (P.R. China)
E-mail: txliu@fudan.edu.cn

[b] Dr. W. Fan, Prof. T. Liu
State Key Laboratory for Modification of Chemical Fibers and Polymer Materials, College of Materials Science and Engineering
Donghua University, Shanghai 201620 (P. R. of China)
E-mail: weifan@dhu.edu.cn

Supporting Information for this article can be found under: http://dx.doi.org/10.1002/celc.201600183.

phene.[30] In this regard, by incorporating carbon nanotubes (CNTs) between graphene sheets to form sandwich-type structures, the restacking of graphene sheets is effectively inhibited while graphene sheets can simultaneously prevent the aggregation of CNTs.[31–33] Furthermore, the incorporated CNTs can be utilized as spacers and conductive linkers between individual graphene sheets, thereby forming three-dimensional (3D) nanoporous graphene/CNT hybrids with greatly enhanced specific surface area and electrical conductivity compared with bare graphene sheets.[34] Thus, nitrogen-doped graphene/CNT hybrids are expected to be ideal templates for immobilization and confinement of electrochemically active electrode materials.

Herein, we report for the first time a facile, one-step process to prepare 3D hierarchically nanostructured composites ($NiCo_2S_4$/NGC) of ultrathin $NiCo_2S_4$ nanosheets grown on N-doped graphene/CNT (NGC) matrices for highly reversible lithium storage. In this composite, $NiCo_2S_4$ nanosheets are uniformly dispersed and confined within the N-doped graphene/CNT frameworks, which can effectively release the strain caused by volumetric change, thus maintaining the overall structural integrity and electrochemical cycling stability. The highly conductive NGC networks with 3D porous structures can facilitate the diffusion of lithium ions to access active materials, and enable rapid transportation of charge to achieve fast lithiation/delithiation process. As a consequence, the resulting $NiCo_2S_4$/NGC hybrids as anode materials exhibit high reversible capacity of 1225.4 mA h g^{-1} at a current density of 0.2 A g^{-1} with excellent cyclic stability and high-rate capability, making them promising anode materials for next-generation LIBs.

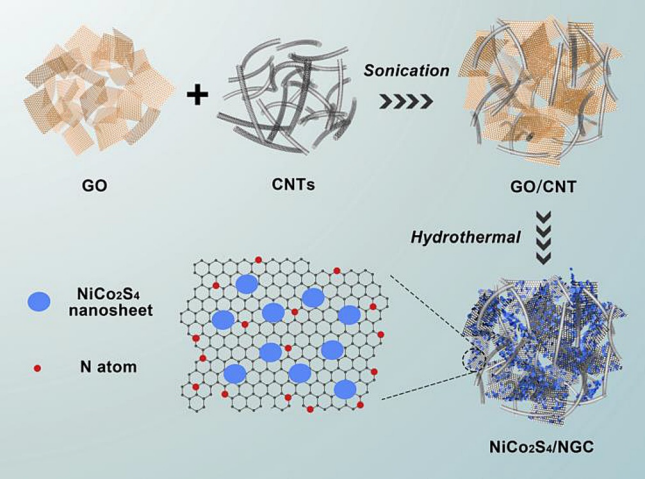

Figure 1. Schematic illustration of the preparation of 3D porous $NiCo_2S_4$/N-doped graphene/CNT ($NiCo_2S_4$/NGC) hybrids.

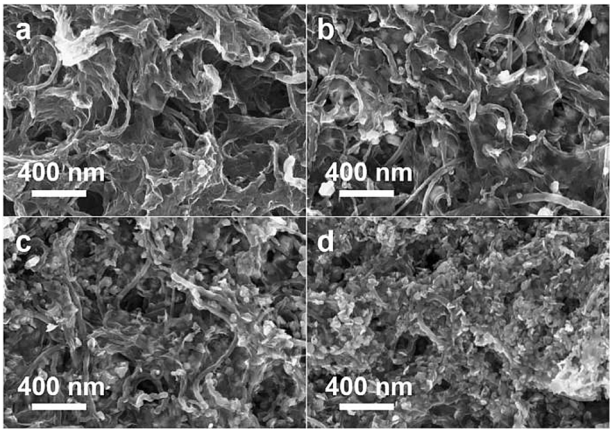

Figure 2. FESEM images of a) NGC, b) $NiCo_2S_4$/NGC-1, c) $NiCo_2S_4$/NGC-2, and d) $NiCo_2S_4$/NGC-3 hybrids.

2. Results and Discussion

2.1. Morphology and Structure of $NiCo_2S_4$/NGC Hybrids

From the TEM image of graphene oxide/carbon nanotube (GO/CNT) hybrids (Figure S1, Supporting Information), pristine CNTs are randomly anchored on the thin GO sheets and no individual GO sheets or CNTs are observed, suggesting the strong π-π stacking interactions between GO sheets and pristine CNTs. During the formation of GO/CNT hybrids, GO sheets can effectively hinder the aggregation of pristine CNTs, and the CNTs can simultaneously prevent the restacking of GO sheets. It is supposed that the π-conjugated multiple aromatic regions of GO sheets can interact with the sidewalls of CNTs through the π-π stacking interactions, whereas the hydrophilic oxygen groups of GO sheets can maintain excellent water dispersibility of GO/CNT hybrids. By employing GO/CNT hybrids as templates, $NiCo_2S_4$/NGC hybrids were easily prepared through a facile, one-step hydrothermal procedure (Figure 1), which is more efficient than those multistep methods reported previously that involved costly, complex, and time-consuming sulfidation processes.[35,36] The morphologies and structures of $NiCo_2S_4$/NGC hybrids were investigated by field-emission scanning electron microscopy (FESEM) (Figure 2). All the $NiCo_2S_4$/NGC hybrids possess 3D hierarchical structures with multiscale pores in the range from several nanometers to several micrometers, which is favorable for fast diffusion of lithium ions to reach active materials.[37] Moreover, the content of $NiCo_2S_4$ nanosheets in $NiCo_2S_4$/NGC hybrids is controllable, and clearly increases as the concentrations of hydrothermal solutions increase (see Experimental Section for details). As shown in Figure 2c, for the $NiCo_2S_4$/NGC-2 hybrid, ultrathin $NiCo_2S_4$ nanosheets are homogeneously dispersed and confined within the 3D porous graphene/CNT networks, which can effectively prevent the self-aggregation of $NiCo_2S_4$ nanosheets. However, excessive amount of $NiCo_2S_4$ nanosheets in $NiCo_2S_4$/NGC-3 hybrid will result in serious agglomeration (Figure 2d). Besides, as shown in Figure S2, the FESEM image and corresponding EDX mapping images of $NiCo_2S_4$/NGC-2 hybrid reveal the homogeneous distribution of carbon, nickel, cobalt, sulfur and nitrogen elements, which also confirmes that $NiCo_2S_4$ nanosheets are uniformly dispersed in the nitrogen-doped graphene/CNT matrices. Based on the thermogravimetric (TGA) tests (Figure S3), the weight ratios of $NiCo_2S_4$ in the hybrids can be calculated from the residual fractions of the samples. The weight ratios of

$NiCo_2S_4$ are 56, 72, 86, and 67% in $NiCo_2S_4$/NGC-1, $NiCo_2S_4$/NGC-2, $NiCo_2S_4$/NGC-3, and $NiCo_2S_4$/NG-2 hybrids, respectively.

The detailed nanostructures of $NiCo_2S_4$/NGC-2 hybrid were further investigated by transmission electron microscopy (TEM). As shown in Figure 3a, the graphene sheets are thin

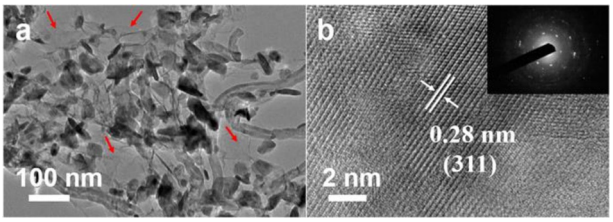

Figure 3. a) TEM and b) HRTEM images of $NiCo_2S_4$/NGC-2 hybrid. The inset of b) shows the corresponding SAED pattern of $NiCo_2S_4$ nanosheets grown on the $NiCo_2S_4$/NGC-2 hybrid.

and slightly scrolled on the sheet edges (pointed out by red arrows). The pristine CNTs are randomly anchored on the surface of graphene sheets whereas $NiCo_2S_4$ nanosheets are uniformly dispersed in the graphene/CNT matrices. The confinement of $NiCo_2S_4$ nanosheets within graphene/CNT hybrids can effectively prevent them from aggregation and inhibit their volumetric expansion during the lithiation/delithiation process. Furthermore, the morphological similarity between two-dimensional $NiCo_2S_4$ nanosheets and graphene sheets can increase the electrical contact areas for rapid transfer of lithium ions and electrons across the interfaces. The HRTEM image of $NiCo_2S_4$/NGC-2 hybrid and the corresponding selected-area electron diffraction (SAED) pattern of $NiCo_2S_4$ nanosheets are displayed in Figure 3b. Lattice fringes with lattice spacing of 0.28 nm can be observed, which corresponds to the (311) plane of $NiCo_2S_4$. The SAED pattern reveals the polycrystalline nature of $NiCo_2S_4$ nanosheets. These results unambiguously confirm the existence of $NiCo_2S_4$ nanosheets in $NiCo_2S_4$/NGC hybrids.

The crystal structures of GO, CNTs, GO/CNT hybrids, pure $NiCo_2S_4$, NGC, and $NiCo_2S_4$/NGC-2 hybrids were studied using X-ray diffraction (XRD) (Figure 4). GO displays a typical diffraction peak at $2\theta = 10.6^\circ$ as a result of the introduction of oxy-

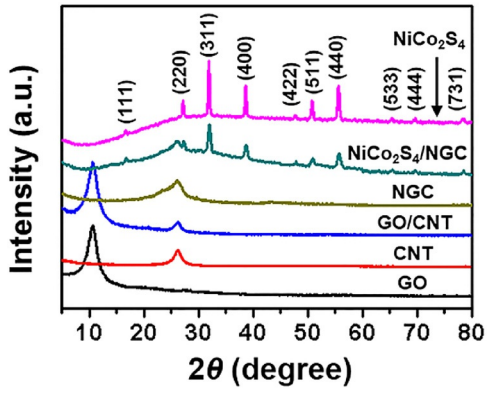

Figure 4. XRD patterns of GO, CNT, GO/CNT, $NiCo_2S_4$, NGC, and $NiCo_2S_4$/NGC hybrids.

genated functional groups on graphene sheets, and pristine CNTs show a characteristic diffraction peak at $2\theta = 26.2^\circ$. Two clear diffraction peaks at $2\theta = 10.6^\circ$ and 26.2° are observed in the XRD pattern of GO/CNT hybrids, indicating the combination of GO and CNTs. For the NGC hybrids, the diffraction peak at $2\theta = 10.6^\circ$ disappears, which confirms the successful reduction of GO to graphene.[29] Bare $NiCo_2S_4$ nanosheets show ten diffraction peaks at $2\theta = 16.6^\circ$, 27.1°, 31.9°, 38.6°, 47.7°, 50.8°, 55.6°, 65.4°, 69.6°, and 78.5°, which can be indexed to (111), (220), (311), (400), (422), (511), (440), (533), (444), and (731) planes of $NiCo_2S_4$ (JCPDS 20–0782), respectively.[21] The XRD pattern of the $NiCo_2S_4$/NGC-2 hybrid exhibits a combination of both NGC and $NiCo_2S_4$ nanosheets and no clear peaks from the impurity phase are observed, suggesting the co-existence of graphene, CNTs, and $NiCo_2S_4$ in the hybrids.

The surface electronic state and composition of $NiCo_2S_4$/NGC-2 hybrid were further investigated by X-ray photoelectron spectroscopy (XPS) analysis (Figure 5). The survey spectrum of $NiCo_2S_4$/NGC-2 hybrid (Figure 5a) reveals the existence of C, Ni, Co, S, N, and O elements in the $NiCo_2S_4$/NGC-2 hybrid, and no detectable impurity is observed. Moreover, the nitrogen atomic content of $NiCo_2S_4$/NGC-2 hybrid is found to be 7.6%. The high-resolution spectrum of Co 2p (Figure 5b) shows two peaks at 793.6 and 778.6 eV, which are ascribed to the Co $2p_{1/2}$ and Co $2p_{3/2}$ binding energies, respectively. In the high-resolution Ni 2p spectrum (Figure 5c), two strong main peaks located at 870.2 and 852.9 eV as well as their associated satellite peaks at 875.2 and 856.8 eV can be attributed to the Ni $2p_{1/2}$ and Ni $2p_{3/2}$ binding energies, respectively. From the high-resolution S 2p spectrum (Figure 5d), two peaks at 162.5 and 161.3 eV can be observed, which are related to S $2p_{1/2}$ and S $2p_{3/2}$ orbitals of divalent sulfide ions (S^{2-}), respectively. These XPS results are in good agreement with those reported previously for $NiCo_2S_4$.[38–40] From the N 1s spectrum (Figure 5e), the peak deconvolution suggests three components centered at 398.5, 400.1, and 401.5 eV, corresponding to pyridinic-N (*N*-6), pyrrolic-N (*N*-5), and quaternary-N (*N*-Q), respectively.[29] The percentages of *N*-6, *N*-5, and *N*-Q are estimated to be 52.1, 44.6, and 3.3%, respectively. According to the previous studies, the presence of pyridinic and pyrrolic forms of nitrogen in graphene sheets is favorable for enhancing the electronic properties of graphene.[29] The pyridinic nitrogen can provide a lone electron pair for conjugation with the π-conjugated rings whereas pyrrolic nitrogen is able to improve the charge mobility in the carbon matrix by introducing electron-donor characteristics, thus facilitating the rapid electron-transfer reactions.[28] High-resolution C 1s spectra of the GO/CNT and $NiCo_2S_4$/NGC-2 hybrids are presented in Figure S4 and Figure 5f, respectively. From the C 1s spectrum of GO/CNT hybrid (Figure S4), five different peaks centered at 284.5, 285.3, 286.8, 287.8, and 288.7 eV are observed, corresponding to sp^2 C, sp^3 C, –C–O, –C=O, and –COO groups, respectively.[41] By comparison, the intensities of C 1s peaks for the carbon binding to oxygen (–C–O, –C=O and –COO groups) decrease remarkably for $NiCo_2S_4$/NGC-2 hybrid (Figure 5f), indicating that most of the oxygen-containing functional groups on the graphene sheets are removed.[41]

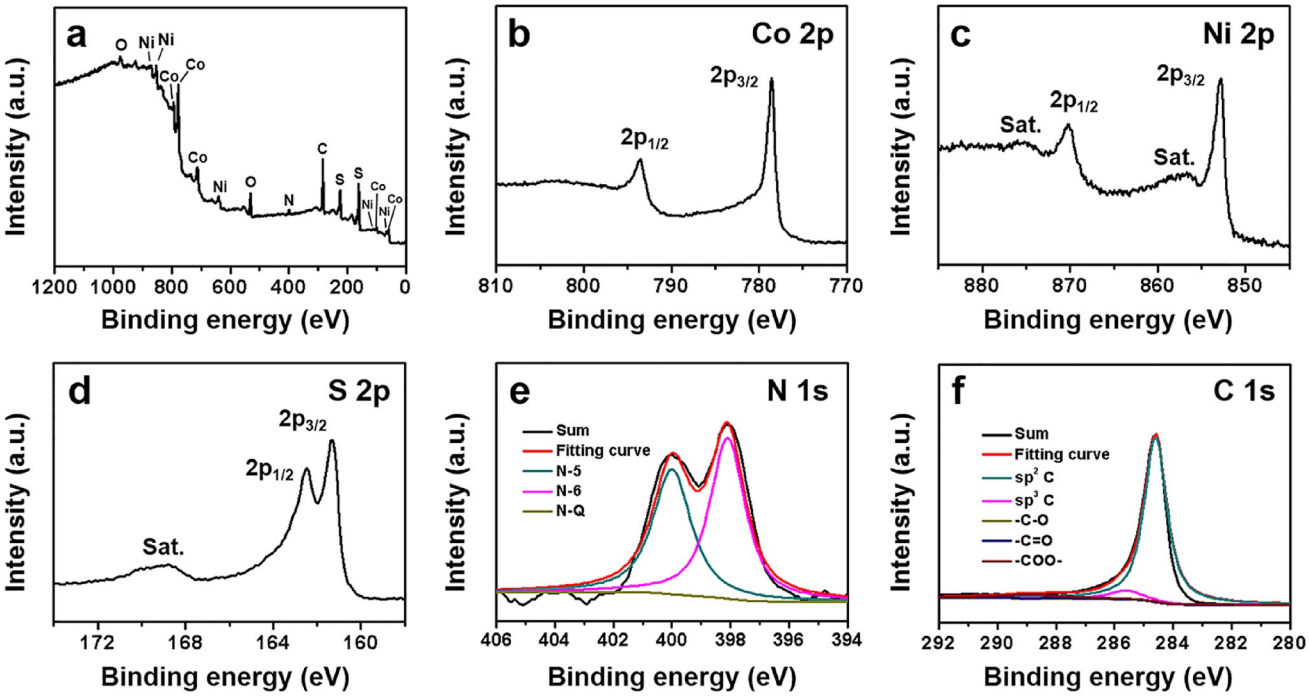

Figure 5. a) XPS survey spectrum, high-resolution b) Co 2p spectrum, c) Ni 2p spectrum, d) S 2p spectrum, e) N 1s spectrum and f) C 1s spectrum of the $NiCo_2S_4$/NGC-2 hybrid.

To further investigate the porous structure and specific surface area of $NiCo_2S_4$/NGC-2 hybrid, Brunauer–Emmett–Teller (BET) analysis of the nitrogen adsorption/desorption isotherms was performed. As displayed in Figure 6, pure $NiCo_2S_4$ displays reversible type II isotherms, which is an indication of nonporous materials. In contrast, both the $NiCo_2S_4$/NG-2 and $NiCo_2S_4$/NGC-2 hybrids exhibit type IV isotherms with typical H2 hysteresis loops, verifying the mesoporous nature of the materials. The specific surface areas of $NiCo_2S_4$, $NiCo_2S_4$/NG-2, and $NiCo_2S_4$/NGC-2 hybrids are summarized in Table S1. Notably, the specific surface areas of $NiCo_2S_4$/NGC-2 and $NiCo_2S_4$/NG-2 hybrids are 168.6 and 106.2 $m^2 g^{-1}$, respectively, which directly reveals that the incorporation of CNTs can significantly increase the porosity and specific surface area. The specific surface area of $NiCo_2S_4$/NGC-2 hybrid is nearly 12 times higher than that of bare $NiCo_2S_4$ nanosheets (14.1 $m^2 g^{-1}$). This is mainly attributed to the 3D porous architectures derived from the graphene/CNT hybrid frameworks with open and continuous channels. Furthermore, the pore-size distribution of $NiCo_2S_4$/NGC-2 hybrid calculated from the Barrett–Joiner–Halenda method is mainly centered at about 4 nm (inset of Figure 6), which is in the mesoporous range. Porous structures with higher specific surface area are advantageous for electrode materials, which can facilitate rapid diffusion of lithium ions to access active materials and accommodate the volumetric expansion of active materials during the lithiation/delithiation process.[42–44]

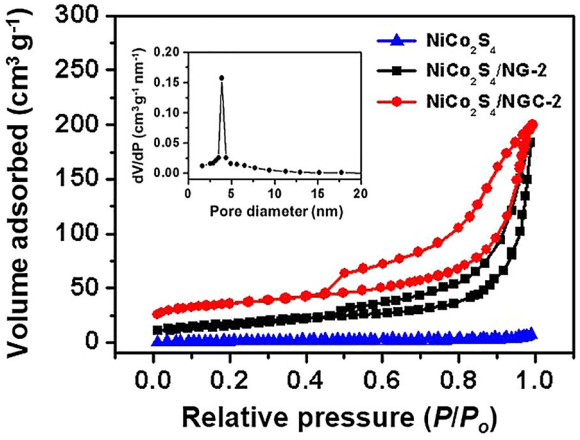

Figure 6. Nitrogen adsorption/desorption isotherms of $NiCo_2S_4$, $NiCo_2S_4$/NG-2, and $NiCo_2S_4$/NGC-2 hybrids. The inset shows the corresponding pore-size distribution of $NiCo_2S_4$/NGC-2 hybrid.

2.2. Electrochemical Performance of $NiCo_2S_4$/NGC Hybrids

To investigate the electrochemistry during the cell testing process, cyclic voltammetry (CV) curves of the 1st, 2nd, and 5th cycles of $NiCo_2S_4$/NGC-2 hybrid was collected in the potential window from 0.01 to 3.0 V at a scan rate of 0.1 $mV s^{-1}$ (Figure 7a). In the initial cathodic scan, the reduction peak located at 1.1 V is ascribed to the conversion reaction of Li^+ with $NiCo_2S_4$ to form metallic Ni and Co nanoparticles embedded in the Li_2S matrix [Eq. (1)]. The small reduction peak at about 0.6 V appears due to the formation of a solid electrolyte interface (SEI) layer.[32] In the first and subsequent anodic scans, the oxidation peaks located at 2.05 and 2.37 V can correspond to the oxidation of metallic Ni and Co to NiS_x and CoS_x, respectively.[24] During the subsequent cathodic scans, the reduction peaks observed at 1.23 and 1.68 V are attributed to the reduc-

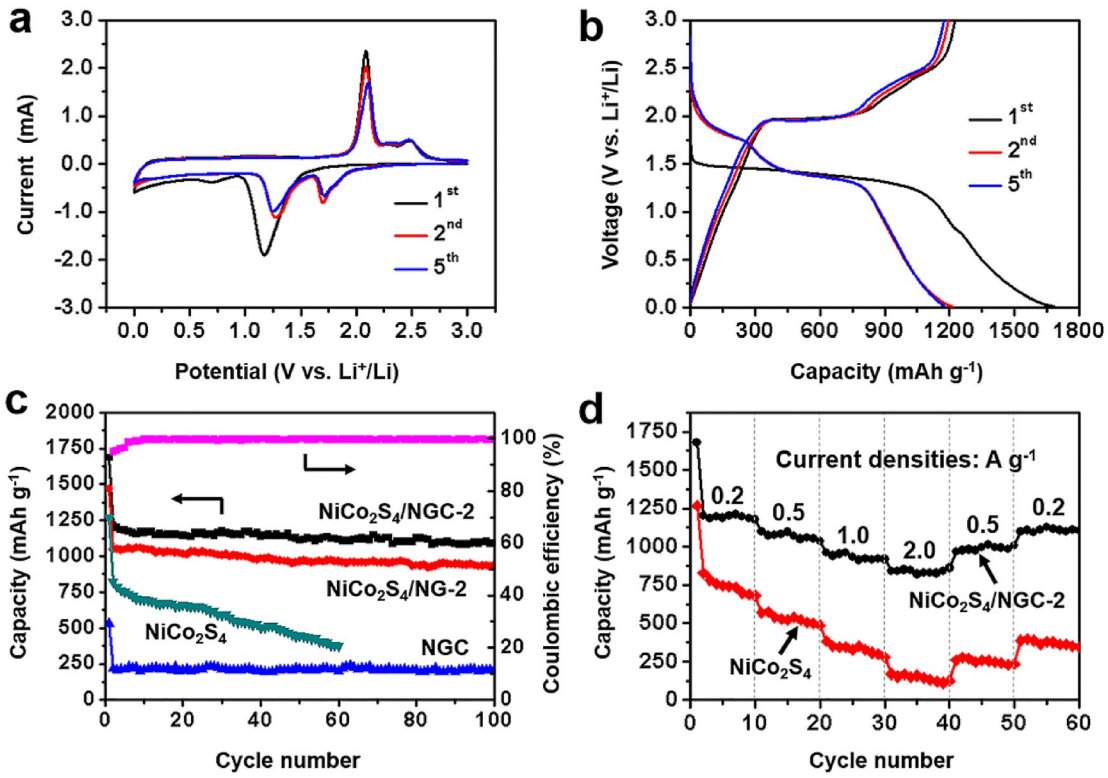

Figure 7. a) CV curves of $NiCo_2S_4$/NGC-2 hybrid at a scan rate of 0.1 mV s^{-1}. b) Discharge/charge curves of $NiCo_2S_4$/NGC-2 hybrid in the 1st, 2nd, and 5th cycles. c) Cycling performance of $NiCo_2S_4$, NGC, $NiCo_2S_4$/NG-2, and $NiCo_2S_4$/NGC-2 hybrids at a current density of 0.2 A g^{-1}, and the Coulombic efficiency of $NiCo_2S_4$/NGC-2 hybrids. d) Rate performance of bare $NiCo_2S_4$ and $NiCo_2S_4$/NGC-2 electrodes at various current densities.

tion of NiS_x and CoS_x into metallic Ni and Co, respectively.[15] Therefore, the lithiation/delithiation process of $NiCo_2S_4$/NGC hybrids can be explained by considering Equations (2) and (3):

$$NiCo_2S_4 + 8\,Li^+ + 8\,e^- \rightarrow Ni + Co + 4\,Li_2S \quad (1)$$

$$Ni + x\,Li_2S \rightleftharpoons NiS_x + 2x\,Li^+ + 2x\,e^- \quad (2)$$

$$Co + x\,Li_2S \rightleftharpoons CoS_x + 2x\,Li^+ + 2x\,e^- \quad (3)$$

Figure 7b shows the galvanostatic discharge-charge profiles (1st, 2nd, and 5th cycles) of the $NiCo_2S_4$/NGC-2 hybrid at a current density of 0.2 A g^{-1}. There is one potential plateau located at 1.4 V in the first discharge curve, corresponding to the lithiation of $NiCo_2S_4$ into Ni and Co nanoparticles embedded in the Li_2S matrix, which is in accordance with the CV results. The potential plateaus located at approximately 1.7 and 1.3 V in the subsequent discharge curves as well as the potential plateaus located at around 2.0 and 2.4 V in the charge curves are attributed to the reversible conversion reactions of metallic Ni and Co into NiS_x and CoS_x [Eqs. (2) and (3)], which also agrees well with the CV tests. In contrast, only one flat potential plateau at about 0.25 V in the first discharge curve is observed for bare NGC hybrids, and the plateaus mentioned above for $NiCo_2S_4$/NGC-2 hybrid cannot be observed (Figure S5, see the Supporting Information). Benefiting from the conductive pathway of NGC networks as well as the redox reactions provided by both nickel and cobalt ions, high initial discharge and charge capacities of 1687.2 and 1225.4 mA h g^{-1} are achieved for the $NiCo_2S_4$/NGC-2 hybrid, with initial Columbic efficiency of 55%. Notably, the irreversible capacity loss during the first cycle is inevitable, which is due to the formation of the SEI layer resulting from electrochemically driven electrolyte degradation.[32]

Not only high reversible capacity but also good cycling stability are desirable for promising anode materials in next-generation LIBs. Figure 7c demonstrates the cycling performance of $NiCo_2S_4$, NGC, $NiCo_2S_4$/NG-2, and $NiCo_2S_4$/NGC-2 electrodes at a current density of 0.2 A g^{-1}. From the results of cycling tests, the NGC hybrid exhibits excellent cycling stability, but its reversible capacity is only 220 mA h g^{-1}. Although the $NiCo_2S_4$ electrode exhibits high initial capacity of 821.8 mA h g^{-1}, it shows severe capacity fade and only delivers a specific capacity of 235.6 mA h g^{-1} after 60 cycles, which results from serious self-aggregation and pulverization during the long-term lithiation/delithiation process. In contrast, the $NiCo_2S_4$/NGC-2 electrode exhibits remarkably enhanced electrochemical performance with high initial charge capacity of 1225.4 mA h g^{-1} at a current density of 0.2 A g^{-1} and retains 1090.6 mA h g^{-1} after 100 cycles, achieving 89% capacity retention of its initial capacity. In addition, the Columbic efficiency of $NiCo_2S_4$/NGC-2 electrode gradually achieves nearly 100% after several cycles, indicating its excellent cyclic stability upon long-term cycling. As shown in Figure S6 (see the Supporting Information), the specific capacity of $NiCo_2S_4$/NGC-3 electrode shows continuous decay, which exhibits high initial charge capacity of 1133.9 mA h g^{-1} at a current density of 0.2 A g^{-1} and only re-

tains 58% capacity retention of its initial capacity after 100 cycles. In contrast, the $NiCo_2S_4$/NGC-1 electrode shows improved stability, with 90% capacity retention after 100 cycles, but its specific capacity is much lower than that of the $NiCo_2S_4$/NGC-2 electrode. Among all the $NiCo_2S_4$/NGC electrodes, the $NiCo_2S_4$/NGC-2 electrode delivers the highest reversible capacity after 100 cycles, which can be attributed to the optimized amount of $NiCo_2S_4$ nanosheets confined within the conductive NGC frameworks as well as to a better electrical contact and interfacial interaction between $NiCo_2S_4$ nanosheets and NGC hybrid. Additionally, the NGC matrix can buffer the volume expansion during the lithiation/delithiation reactions and restrain the agglomeration of $NiCo_2S_4$ nanosheets during the long-term cycling tests, leading to significantly enhanced cyclic stability of $NiCo_2S_4$/NGC-2 electrode. Notably, the $NiCo_2S_4$/NGC-2 electrode exhibits higher reversible capacities than $NiCo_2S_4$/NG-2 electrode, indicating the significance of conductive CNTs incorporated between graphene sheets. Associated with the morphology analysis and BET results, the incorporation of CNTs can effectively prevent the restacking of graphene sheets, provide 3D conductive networks for fast charge transfer and increase the porosity for rapid diffusion of lithium ions, thus resulting in greatly enhanced lithium storage performance. As displayed in Table S2, the specific capacity of $NiCo_2S_4$/NGC-2 hybrid is much larger than those of $NiCo_2O_4$-based anode materials and most of the $NiCo_2O_4$-based anode materials when considering the same current density and cycling number.

The rate capabilities of bare $NiCo_2S_4$ and $NiCo_2S_4$/NGC-2 electrode were investigated at various current densities (Figure 7d). The specific capacity of bare $NiCo_2S_4$ electrode fades to less than 130 mA h g^{-1} as the current density increases to 2 A g^{-1}, and regains a capacity of about 346.2 mA h g^{-1} (only ca. 42% of the initial charge capacity) when the current density decreases back to 0.2 A g^{-1}. In contrast, the $NiCo_2S_4$/NGC-2 electrode delivers a high reversible capacity of 830 mA h g^{-1} as the current density increases to 2 A g^{-1}. Moreover, the reversible capacity restores to 1103.5 mA h g^{-1} when the current rate is changed back to 0.2 A g^{-1}, approaching 92% of its initial charge capacity. Furthermore, the capacities of the $NiCo_2S_4$/NGC-2 hybrid can be retained at 920.8, 807.2, and 574.8 mA h g^{-1} at 1, 2, and 5 A g^{-1} after 100 cycles, respectively, indicating its outstanding cyclic stability at high current densities (Figure 8). As shown in the postmortem FESEM image of $NiCo_2S_4$/NGC-2 hybrid after the cycling tests (Figure S7), $NiCo_2S_4$ nanosheets are still uniformly confined within the NGC matrix, and the 3D porous structures of $NiCo_2S_4$/NGC-2 hybrid are maintained. In sharp contrast, for the $NiCo_2S_4$ electrode, $NiCo_2S_4$ nanosheets severely aggregate into large agglomerates after the cycling tests. These results confirm that the NGC networks can effectively prevent $NiCo_2S_4$ nanosheets from aggregation and maintain the overall structures of $NiCo_2S_4$/NGC-2 hybrid. Benefiting from the synergistic effects between $NiCo_2S_4$ nanosheets and NGC frameworks, the hierarchical nanostructures of $NiCo_2S_4$/NGC hybrids can significantly shorten the diffusion length of lithium ions, facilitating the charge transfer with little resistance as well as preventing $NiCo_2S_4$ nanosheets from aggregation and pulverization, all contributing to the remarkably enhanced cyclic stability and rate capability of $NiCo_2S_4$/NGC hybrids.

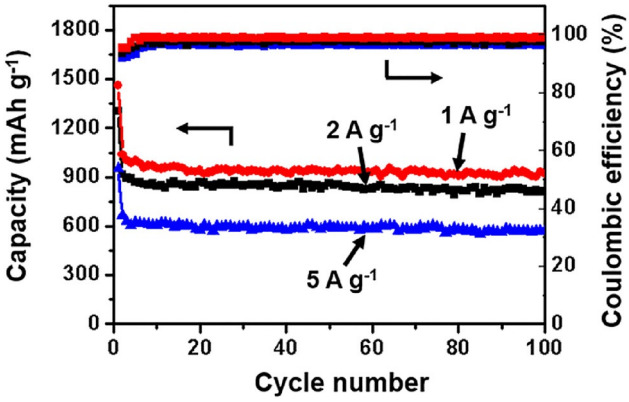

Figure 8. High-rate cycling performance and the Coulombic efficiency of $NiCo_2S_4$/NGC-2 hybrid in the voltage range from 0.01 to 3.0 V at current densities of 1, 2, and 5 A g^{-1}, respectively.

To better understand the superior electrochemical performance of $NiCo_2S_4$/NGC hybrids, electrochemical impedance spectroscopy (EIS) analyses were carried out to study the electrochemical impedance of bare $NiCo_2S_4$, $NiCo_2S_4$/NG-2, and $NiCo_2S_4$/NGC-2 hybrids (Figure 9). In general, the Nyquist plot

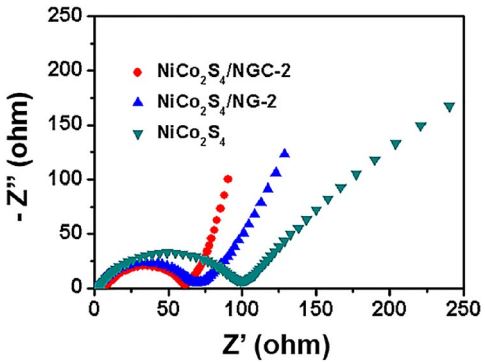

Figure 9. Nyquist plots of $NiCo_2S_4$, $NiCo_2S_4$/NG-2, and $NiCo_2S_4$/NGC-2 hybrids.

consists of a semicircle in the high-frequency region and a straight line in the low-frequency region, corresponding to the charge-transfer resistance and ion-diffusion resistance in the electrode, respectively.[35] It can be clearly seen that the $NiCo_2S_4$/NGC-2 electrode displays a much smaller radius of semicircle in the high-frequency region compared with that of the bare $NiCo_2S_4$ electrode, which indicates that the $NiCo_2S_4$/NGC-2 electrode possesses much lower charge-transfer resistance at the electrode/electrolyte interfaces. Furthermore, the $NiCo_2S_4$/NGC-2 electrode exhibits a more vertical line than bare $NiCo_2S_4$ electrode in the low-frequency region, illustrating its lower diffusion resistance of ions. These results confirm that the NGC frameworks are able to facilitate rapid transfer of electrons and enable fast diffusion of lithium ions during lithiation/delithiation process, thus resulting in remarkably improved

electrochemical performance. Furthermore, the $NiCo_2S_4$/NGC-2 electrode has smaller diameter of semicircle at high frequencies and more vertical line at low frequencies compared with those of the $NiCo_2S_4$/NG-2 electrode, confirming its significantly decreased resistance for charge transfer and ion diffusion due to the incorporation of CNTs. The incorporated CNTs serve as conductive linkers between individual graphene sheets to form conductive NGC networks, which leads to greatly enhanced electrical conductivity and lithium storage performance of the $NiCo_2S_4$/NGC-2 hybrid.

3. Conclusions

We have demonstrated an efficient one-step synthesis of hierarchically nanostructured $NiCo_2S_4$/NGC hybrids as novel anode materials for high-performance LIBs. The optimized $NiCo_2S_4$/NGC hybrid with 3D hierarchical nanostructures of ultrathin $NiCo_2S_4$ nanosheets uniformly confined within N-doped graphene/CNT networks provides rapid pathways for charge transfer and ion diffusion, and exhibits high reversible capacity and excellent cycling stability. The present encouraging results suggest that nanostructured $NiCo_2S_4$ and other ternary sulfides have great potential as advanced anode materials for applications in LIBs. These innovative $NiCo_2S_4$/NGC hybrids, with remarkably improved electrochemical performance, could be further explored as promising anode materials for high-performance LIBs.

Experimental Section

Materials

Natural graphite powder (325 meshes) was purchased from Alfa-Aesar. Pristine carbon nanotubes were supplied by Chengdu Institute of Organic Chemistry, Chinese Academy of Sciences. All other reagents were purchased from Sinopharm Chemical Reagent Co. Ltd. and used as received without further purification. Deionized water was used throughout all the experiments.

Preparation of GO/CNT Hybrid Suspension

Graphene oxide (GO) was synthesized from natural graphite powder by a modified Hummers method.[45] The resulting GO solid was dispersed in water by sonication under ambient conditions for 30 min to make a homogeneous GO aqueous dispersion. Stable aqueous suspension of GO/CNT hybrids were prepared by using our previously reported method.[46] Briefly, pristine CNTs are added into the aqueous dispersion of GO sheets with GO to CNT weight ratio of 2:1, then the mixture was sonicated (at 60 W) under ambient conditions for 30 min. The mixed suspension was centrifuged for 5 min at 6000 rpm to remove the unstabilized CNTs, thus obtaining a homogeneous and stable GO/CNT hybrid suspension.

Preparation of $NiCo_2S_4$/N-Doped Graphene/CNT Hybrids

As shown in Figure 1, the $NiCo_2S_4$/N-doped graphene/CNT hybrids ($NiCo_2S_4$/NGC) were prepared through a facile one-step hydrothermal procedure. Typically, the designed amount of $Ni(NO_3)_2{\cdot}6H_2O$ (0.5, 1 and 2 mmol) with the corresponding amount of $Co(NO_3)_2{\cdot}6H_2O$ (1, 2 and 4 mmol) and thiourea (2, 4 and 8 mmol) were added to 30 mL GO/CNT hybrid suspension (0.5 mg mL^{-1}). Then, ethylenediamine (2 mL) and 25% NH_4OH (2 mL) were slowly added into the suspension. The mixture was sonicated for 10 min and then transferred to a 50 mL Teflon-lined autoclave for heat treatment at 200 °C for 16 h. After the reaction system cooled to RT naturally, the black precipitate was washed with deionized water and ethanol several times and dried at 60 °C under vacuum. The as-prepared $NiCo_2S_4$/NGC hybrids with different amounts of $NiCo_2S_4$ were named $NiCo_2S_4$/NGC-1, $NiCo_2S_4$/NGC-2, and $NiCo_2S_4$/NGC-3, respectively. For the control experiments, bare N-doped graphene/CNT hybrids (NGC) and $NiCo_2S_4$/N-doped graphene hybrids ($NiCo_2S_4$/NG) were also prepared by using a similar process. Bare $NiCo_2S_4$ nanosheets ($NiCo_2S_4$) are also prepared without any GO/CNT hybrid suspension.

Characterization

The morphologies of the samples were investigated by using field-emission scanning electron microscope (FESEM, Ultra 55, Zeiss) at an acceleration voltage of 5 kV. Transmission electron microscopy (TEM) and high-resolution transmission electron microscopy (HRTEM) observation were performed with Tecnai G2 20 TWIN TEM under an acceleration voltage of 200 kV. All the TEM samples were first dispersed in aqueous solutions through sonication to form a homogenous suspension. The TEM samples were then prepared by dropping the suspension on the copper grids and drying in air. X-ray diffraction (XRD) patterns of the samples were conducted with an X'Pert Pro X-ray diffractometer with Cu Kα radiation ($\lambda =$ 0.1542 nm) under a voltage of 40 kV and a current of 40 mA. X-ray photoelectron spectroscopy (XPS) analyses were made with a VG ESCALAB 220I-XL device. All XPS spectra were corrected by using the C 1s line at 284.5 eV and the curve fitting was accomplished by using XPS Peak 4.1 software. The Brunauer–Emmett–Teller (BET) surface area was measured with a Belsorp-max surface area detecting instrument by N_2 physisorption at 77 K. Thermogravimetric analysis (TGA, Pyris 1) was performed under air flow from 50 to 800 °C at a heating rate of 10 °C min^{-1}.

Electrochemical Measurements

The electrochemical measurements were carried out in 2025 coin cells assembled in an argon-filled glovebox (M.Braun Inertgas Systems Co. Ltd.) with the concentrations of moisture and oxygen below 0.1 ppm. Pure lithium foil was used as the counter electrode, and a polypropylene film (Celgard-2400) was used as the separator. The electrolyte consisted of a solution of 1 M $LiPF_6$ in ethylene carbonate (EC)/dimethyl carbonate (DMC)/diethyl carbonate (DEC) (1:1:1 by volume). The working electrodes were prepared by using a slurry coating procedure. The slurry consisted of $NiCo_2S_4$/NGC hybrids, acetylene black, and poly(vinylidene fluoride) dissolved in *N*-methyl-2-pyrrolidinone at a weight ratio of 8:1:1, respectively. The as-prepared slurry was pasted on pure copper foil and dried at 80 °C under vacuum. The mass of NGC, $NiCo_2S_4$, $NiCo_2S_4$/NGC-2, and $NiCo_2S_4$/NG-2 electrodes are approximately 2.05, 2.16, 2.08, and 2.10 mg, respectively. Cyclic voltammetry (CV) curves were collected with a CHI660D electrochemical workstation (Chenhua Instruments Co. Ltd.) in the potential range from 0.01 to 3.0 V at a scan rate of 0.1 mV s^{-1}. The galvanostatic discharge-charge measurements and rate-performance tests under different current densities were performed in the voltage range from 0.01 to 3.0 V at RT by using a CT2013A cell test instrument (LAND Electronic Co. Ltd.). The electrochemical impedance spectroscopy (EIS) was

measured in the frequency range from 100 kHz to 0.01 Hz at open circuit potential with an AC voltage amplitude of 5.0 mV.

Acknowledgements

The authors are grateful for the financial support from the National Natural Science Foundation of China (51125011, 51433001).

Keywords: electron transport · energy conversion · graphene · lithium · nanostructures

[1] Q. F. Zhang, E. Uchaker, S. L. Candelaria, G. Z. Cao, *Chem. Soc. Rev.* **2013**, *42*, 3127 – 3171.
[2] X. H. Cao, Y. M. Shi, W. H. Shi, X. H. Rui, Q. Y. Yan, J. Kong, H. Zhang, *Small* **2013**, *9*, 3433 – 3438.
[3] L. S. Zhang, W. Fan, W. W. Tjiu, T. X. Liu, *RSC Adv.* **2015**, *5*, 34777 – 34787.
[4] H. Wang, H. B. Feng, J. H. Li, *Small* **2014**, *10*, 2165 – 2181.
[5] H. Geng, S. F. Kong, Y. Wang, *J. Mater. Chem. A* **2014**, *2*, 15152 – 15158.
[6] X. Wei, W. H. Li, J. Shi, L. Gu, Y. Yu, *ACS Appl. Mater. Interfaces* **2015**, *7*, 27804 – 27809.
[7] Q. F. Wang, R. Q. Zou, W. Xia, J. Ma, B. Qiu, A. Mahmood, R. Zhao, Y. C. Yang, D. G. Xia, Q. Xu, *Small* **2015**, *11*, 2511 – 2517.
[8] L. F. Shen, J. Wang, G. Y. Xu, H. S. Li, H. Dou, X. G. Zhang, *Adv. Energy Mater.* **2015**, *5*, 1400977.
[9] Y. M. Chen, Z. Li, X. W. Lou, *Angew. Chem. Int. Ed.* **2015**, *54*, 10521 – 10524; *Angew. Chem.* **2015**, *127*, 10667 – 10670.
[10] X. Y. Yu, L. Yu, L. F. Shen, X. H. Song, H. Y. Chen, X. W. Lou, *Adv. Funct. Mater.* **2014**, *24*, 7440 – 7446.
[11] J. W. Xiao, L. Wan, S. H. Yang, F. Xiao, S. Wang, *Nano Lett.* **2014**, *14*, 831 – 838.
[12] X. Y. Yu, L. Yu, X. W. Lou, *Adv. Energy Mater.* **2016**, *6*, 1501333.
[13] F. Zhu, H. Xia, T. Feng, *Mater. Technol.* **2015**, *30*, A53 – A57.
[14] H. C. Chen, J. J. Jiang, L. Zhang, H. Z. Wan, T. Qi, D. D. Xia, *Nanoscale* **2013**, *5*, 8879 – 8883.
[15] D. Bhattacharjya, A. Sinhamahapatra, J. J. Ko, J. S. Yu, *Chem. Commun.* **2015**, *51*, 13350 – 13353.
[16] R. J. Zou, M. F. Yuen, L. Yu, J. Q. Hu, C. S. Lee, W. J. Zhang, *Sci. Rep.* **2016**, *6*, 20264.
[17] M. Sun, J. J. Tie, G. Cheng, T. Lin, S. M. Peng, F. Z. Deng, F. Ye, L. Yu, *J. Mater. Chem. A* **2015**, *3*, 1730 – 1736.
[18] L. F. Shen, L. Yu, H. B. Wu, X. Y. Yu, X. G. Zhang, X. W. Lou, *Nat. Commun.* **2015**, *6*, 6694.
[19] L. Yu, B. Y. Guan, W. Xiao, X. W. Lou, *Adv. Energy Mater.* **2015**, *5*, 1500981.
[20] X. Xu, Z. Y. Fan, X. Y. Yu, S. J. Ding, D. M. Yu, X. W. Lou, *Adv. Energy Mater.* **2014**, *4*, 1400902.
[21] S. J. Peng, L. L. Li, C. C. Li, H. T. Tan, R. Cai, H. Yu, S. Mhaisalkar, M. Srinivasan, S. Ramakrishna, Q. Y. Yan, *Chem. Commun.* **2013**, *49*, 10178 – 10180.
[22] X. H. Xiong, G. Waller, D. Ding, D. C. Chen, B. Rainwater, B. T. Zhao, Z. X. Wang, M. L. Liu, *Nano Energy* **2015**, *16*, 71 – 80.
[23] Y. F. Zhang, C. C. Sun, H. Q. Su, W. Huang, X. C. Dong, *Nanoscale* **2015**, *7*, 3155 – 3163.
[24] R. J. Zou, Z. Y. Zhang, M. F. Yuen, M. L. Sun, J. Q. Hu, C. S. Lee, W. J. Zhang, *NPG Asia Mater.* **2015**, *7*, e195.
[25] L. F. Zhao, Q. Li, R. L. Zhang, X. J. Tian, L. Liu, *Chin. J. Polym. Sci.* **2016**, *34*, 111 – 121.
[26] Y. Q. Sun, Q. O. Wu, G. Q. Shi, *Energy Environ. Sci.* **2011**, *4*, 1113 – 1132.
[27] M. Q. Zhao, X. F. Liu, Q. Zhang, G. L. Tian, J. Q. Huang, W. C. Zhu, F. Wei, *ACS Nano* **2012**, *6*, 10759 – 10769.
[28] Y. Zhao, C. G. Hu, Y. Hu, H. H. Cheng, G. Q. Shi, L. T. Qu, *Angew. Chem. Int. Ed.* **2012**, *51*, 11371 – 11375; *Angew. Chem.* **2012**, *124*, 11533 – 11537.
[29] W. Fan, Y. E. Miao, Y. P. Huang, W. W. Tjiu, T. X. Liu, *RSC Adv.* **2015**, *5*, 9228 – 9236.
[30] S. Y. Yin, Y. Y. Zhang, J. H. Kong, C. J. Zou, C. M. Li, X. H. Lu, J. Ma, F. Boey, X. D. Chen, *ACS Nano* **2011**, *5*, 3831 – 3838.
[31] Z. J. Fan, J. Yan, L. J. Zhi, Q. Zhang, T. Wei, J. Feng, M. L. Zhang, W. Z. Qian, F. Wei, *Adv. Mater.* **2010**, *22*, 3723.
[32] L. S. Zhang, Y. P. Huang, Y. F. Zhang, W. Fan, T. X. Liu, *ACS Appl. Mater. Interfaces* **2015**, *7*, 27823 – 27830.
[33] Y. Chen, S. T. Lu, X. H. Wu, J. Liu, *J. Phys. Chem. C* **2015**, *119*, 10288 – 10294.
[34] C. Zhang, T. X. Liu, *Chin. Sci. Bull.* **2012**, *57*, 3010 – 3021.
[35] W. Chen, C. Xia, H. N. Alshareef, *ACS Nano* **2014**, *8*, 9531 – 9541.
[36] X. H. Xia, C. R. Zhu, J. S. Luo, Z. Y. Zeng, C. Guan, C. F. Ng, H. Zhang, H. J. Fan, *Small* **2014**, *10*, 766 – 773.
[37] L. F. Shen, L. Yu, X. Y. Yu, X. G. Zhang, X. W. Lou, *Angew. Chem. Int. Ed.* **2015**, *54*, 1868 – 1872; *Angew. Chem.* **2015**, *127*, 1888 – 1892.
[38] Z. Y. Zhang, X. G. Wang, G. L. Cui, A. H. Zhang, X. H. Zhou, H. X. Xu, L. Gu, *Nanoscale* **2014**, *6*, 3540 – 3544.
[39] Y. F. Zhang, M. Z. Ma, J. Yang, C. C. Sun, H. Q. Su, W. Huang, X. C. Dong, *Nanoscale* **2014**, *6*, 9824 – 9830.
[40] X. M. Li, Q. G. Li, Y. Wu, M. C. Rui, H. B. Zeng, *ACS Appl. Mater. Interfaces* **2015**, *7*, 19316 – 19323.
[41] Z. J. Fan, W. Kai, J. Yan, T. Wei, L. J. Zhi, J. Feng, Y. M. Ren, L. P. Song, F. Wei, *ACS Nano* **2011**, *5*, 191 – 198.
[42] Y. Liu, J. A. Zhang, S. P. Wang, K. X. Wang, Z. M. Chen, Q. Xu, *New J. Chem.* **2014**, *38*, 4045 – 4048.
[43] L. Yu, L. Zhang, H. B. Wu, X. W. Lou, *Angew. Chem. Int. Ed.* **2014**, *53*, 3711 – 3714; *Angew. Chem.* **2014**, *126*, 3785 – 3788.
[44] R. C. Jin, D. M. Liu, C. P. Liu, G. Liu, *RSC Adv.* **2015**, *5*, 84711 – 84717.
[45] W. S. Hummers, R. E. Offeman, *J. Am. Chem. Soc.* **1958**, *80*, 1339.
[46] C. Zhang, L. L. Ren, X. Y. Wang, T. X. Liu, *J. Phys. Chem. C* **2010**, *114*, 11435 – 11440.

Manuscript received: April 11, 2016
Accepted Article published: June 15, 2016
Final Article published: June 30, 2016